V European Conference on Computational Fluid Dynamics
ECCOMAS CFD 2010
J. C. F. Pereira and A. Sequeira (Eds)
Lisbon, Portugal, 14–17 June 2010

NUMERICAL SIMULATION OF A TWO-PHASE FLOW IN AN OIL FILTER BY COUPLING A LES APPROACH WITH A LAGRANGIAN PARTICLE TRACKING

João P. Pinto[*], Yann Fraigneau[†], Luis A. Oliveira[*], Christian Tenaud[†],

[*] UNIVERSITY OF COIMBRA
MECHANICAL ENGINEERING DEPARTMENT - FCTUC - Polo II
3030-788 COIMBRA
PORTUGAL
e-mail: joao_icaro@yahoo.com, Luis.Adriano@dem.uc.pt

[††] LIMSI CNRS UPR 3251
B.P. 133 91403 ORSAY CEDEX
FRANCE
e-mail: {Christian.Tenaud,Yann.Fraigneau}@limsi.fr

Key words: Blow-by gases; droplets' motion; turbulent flows; LES; Lagragian tracking.

Abstract. *The transport simulation of small oil droplets in blow-by gases of diesel engines requires the accurate prediction of turbulent flow structures, as well as of their influence upon the droplets' motion, within complex geometries. The present study addresses the simulation of such a complex flow by means of a Large Eddy Simulation (LES) for the continuous phase, together with a Lagrangian type formulation, used for the tracking of each individual droplet of the particle phase. As a first step, we limit our analysis to a specific, well known and relatively simple configuration that is described in detail in Tekam[1]. This configuration represents a decanter incorporating two baffles, which is used for the oil droplets filtering of the blow-by gas generated by a diesel engine. LES is performed by applying a mixed scales model (Mansour-Bardina) to the filtered Navier-Stokes equations, in order to account for subgrid scale effects. The resulting set of equations is solved with a prediction-projection[2]. The Lagrangian tracking of each individual particle is performed taking into account the forces influencing the dynamics of the oil droplets in both the unbounded flow and the near wall regions. Our numerical predictions are compared with published results that were obtained using a RANS method for the same physical configuration. These comparisons are seen as an encouraging preliminary evaluation of the present code performance.*

1 INTRODUCTION

Computational Fluid Dynamics (CFD) for two-phase flows is being increasingly applied in practice as an efficient, accessible and affordable way of supporting the design and optimization of industrial processes. Relevant applications include interior dust and particle pollutant control systems, separation processes, pneumatic transport, particle combustion in industrial furnaces or energy converters, sediment transport, erosion, safety and fire suppression systems, among many others.

In numerical simulations of fluid-particle flows, the continuous (fluid) phase is typically modeled via an Eulerian approach, while the dispersed (solid particle) phase is predicted using either an Eulerian or a Lagrangian approach[3, 4]. The Lagrangian approach is well suited for the description of the dispersed phase in the so-called *dilute* fluid-particle flows, in which the particle dynamics is controlled primarily by surface and body forces acting on the particle, rather than by particle-particle collisions or interactions. The turbulent flow of the continuous (fluid) phase may be represented by two-equation, Reynolds stress, algebraic stress, large eddy simulation (LES), direct numerical simulation, or discrete vortex models, as is discussed in a review by Crowe *et al.*[3].

One important practical example of such two-phase flows is the evaluation of the efficiency of an oil straining system, which is used to filter the - typically micronic - oil particles contained in the blow-by gases generated by a motorcar engine. The pollution source materialized by this type of gases has motivated several studies, both experimental[5] and numerical[6]. However, the inherent complexity of the phenomena involved in this problem, namely the particle/wall interaction, or the influence that turbulence exerts upon both the continuous and particulate phases, still requires additional physical insight. The present work aims at being one more step in that direction.

For this dilute fluid-particle flow, a Lagrangian procedure is used in the particle tracking within both the unbounded flow and the near wall regions. In order to capture the turbulent structure with sufficient accuracy, a LES is adopted to model the behavior of the carrier fluid flow. Both approaches are described in the following sections, together with the first tests that were performed in order to verify and validate the present model. This is an ongoing work, of which the preliminary results, here reported, are rather encouraging.

2 NUMERICAL MODELING OF THE CONTINUOUS PHASE

2.1 Governing equations

Considering the low speed regime and neglecting heat transfer for convenience, we assume incompressible fluid flow conditions to hold for the continuous phase. The Navier-Stokes equation set describing the flow dynamics is defined as follows:

- Mass equation

$$\nabla \cdot \mathbf{v} = 0 \,. \tag{1}$$

- Momentum equations

$$\frac{\partial \mathbf{v}}{\partial t} + \nabla \cdot (\mathbf{v} \otimes \mathbf{v}) = \frac{1}{\rho_0}(\nabla \cdot \boldsymbol{\tau} - \nabla P), \tag{2}$$

where t is the time, ρ_0 the uniform and constant density, $\mathbf{v}$ the velocity vector, P the pressure and $\boldsymbol{\tau}$ the Reynolds stress tensor defined as:

$$\boldsymbol{\tau} = -2\mu \mathbf{S}, \tag{3}$$

with the strain rate tensor:

$$\mathbf{S} = \frac{1}{2}(\nabla \mathbf{v} + \nabla^t \mathbf{v}) \tag{4}$$

where μ is the molecular viscosity.

2.2 Numerical formulation

The numerical method used to solve the previous governing equations is based on the usual prediction-correction method which is very similar to the one used by Gadouin et al[7] in the natural convection flow instability studies for instance. The prediction step consists in estimating the velocity field at time $(n+1)\delta t$ from previous time step values of the velocity and the pressure. Let us note that this predicted velocity does not satisfy the divergence-free constraint. Then, the divergence-free velocity field and the pressure field are both updated in the projection step. We first consider the prediction step. The momentum equation set is discretized following a finite volume approach on a staggered structured grid with a second order approximation in time and space. Scalar variables are defined at cell centers whereas vectorial variables are located on cell faces. Convection fluxes and viscous terms are calculated with a second order centered scheme. The time discretization is approximated by a second order backward Euler scheme. An implicit discretization is carried out on the viscous terms to increase the stability limit. The convection fluxes are estimated at time $(n+1)\delta t$ using an Adams-Bashforth extrapolation from results already calculated at times $n\delta t$ and $(n-1)\delta t$. The pressure gradient is written explicitly.

The momentum equation for each velocity component is written as a Helmholtz equation. We obtain:

$$\left(I - \frac{2\delta t}{3}\nabla \cdot \upsilon \nabla\right)\mathbf{v}^* = -\nabla P^n + \mathbf{S}^{n,n-1}. \tag{5}$$

$\mathbf{v}^*$ is the predicted velocity field satisfying equation (5). P^n is the pressure field at time $n\delta t$. $\mathbf{S}^{n,n-1}$ is a source term containing terms defined at time $n\delta t$ and $(n-1)\delta t$ which derived from the time discretization, the explicit part of the viscous terms, and convection fluxes. υ is the fluid kinematic viscosity.

Equations are integrated using an ADI (Alternating Direction Implicit) method[8].

We then use a projection method[2] to ensure the zero divergence of the velocity field and to update the corresponding pressure field. From both mass and momentum equations, we write a Poisson's equation as:

$$\Delta\Phi = \frac{\rho_0}{\Delta t}\nabla \mathbf{v}^* , \tag{6}$$

equipped with Neumann's conditions at boundaries. $\Phi = P^{n+1} - P^n$ and v^* is the non-zero divergence velocity field calculated from the Helmholtz equation integration. For each time-step, this equation is solved with an S.O.R iterative method coupled with a multigrid method in order to increase the converge rate. As far as Φ is known, the pressure field P^{n+1} is updated and the velocity vector is corrected following:

$$\mathbf{v} = \mathbf{v}^* - \frac{\Delta t}{\rho_0}\nabla \mathbf{v}^* . \tag{7}$$

2.3 The large eddy simulation modeling

2.3.1. General presentation

The main benefit of the Large Eddy Simulation (LES) lies in supplying much more information and finer details about the flow features than usual RANS (Reynolds Averaged Navier-stokes equations) methods. Explicit information about the instantaneous spatial structure and the unsteady behavior of the flow allows us to get more accurate results on statistical quantities or to acquire some spectral quantities if needed. Therefore, LES is a relevant method to account for turbulent effects with accuracy in engineering flows even if this approach is CPU time consuming with respect to RANS methods. In the LES framework, turbulent flows are solved on a coarser grid than the one required to describe all the scales of the turbulent spectrum. We consider that any flow quantity can be split in a large scale component $\overline{\phi}$ (which is the resolved part of this quantity and is directly solved on the grid) and a subgrid scale component ϕ''. The classical LES methodology consists in applying an implicit spatial filter to the governing equations (1) and (2). From this filtering procedure, the governing equations for incompressible flows are similar to those showed previously, (1) and (2). However, additional nonlinear terms appear in the momentum equation as a consequence of interactions between subgrid scales. The filtered equations then read:

$$\nabla \cdot \overline{\mathbf{v}} = 0 , \tag{8}$$

$$\frac{\partial \overline{\mathbf{v}}}{\partial t} + \nabla \cdot \left(\overline{\mathbf{v}} \otimes \overline{\mathbf{v}} \right) = \frac{1}{\rho_0}\left(\nabla \cdot \overline{\boldsymbol{\tau}}_t + \nabla \cdot \overline{\boldsymbol{\tau}} - \nabla \overline{P} \right), \tag{9}$$

where $\overline{\boldsymbol{\tau}}_t$ is the subgrid stress tensor which is defined as:

$$\overline{\boldsymbol{\tau}}_t = -\rho_0 \left(\overline{\mathbf{v} \otimes \mathbf{v}} - \overline{\mathbf{v}} \otimes \overline{\mathbf{v}} \right). \tag{10}$$

Following a Boussinesq approximation, this term can be modeled by:

$$\overline{\boldsymbol{\tau}}_t = -2\mu_t \overline{\mathbf{S}} , \tag{11}$$

where μ_t stands for the subgrid viscosity.

Numerous LES models of μ_t have been developed and can be found in the literature. For instance, we can cite the well-known Smagorinsky model[9] or equivalently the vorticity model[10]. This kind of models is very popular thanks to its low time consuming and easy implementation. But they show a too high dissipative effect, particularly in regions where the dissipative length scale is greater than the filter cut-off length, including areas where the whole spectrum of turbulent scales is resolved. More accurate and sophisticated models have been developed including a dynamical procedure [11]. However, these models are time consuming and it is delicate to use them when dealing with complex configuration flows. In some cases, they can generate a wrong subgrid behavior, or worst, numerical instabilities. In this study, we choose to use the mixed scale model which is a good compromise between the Smagorinsky model and the dynamical procedure regarding the accuracy as well as the CPU time consumption.

2.3.2. Mixed scale model

The mixed scale model was developed to improve the behavior of the vorticity model in the specific regions mentioned above. This model was first introduced by Ta Phuoc[12] and used by Sagaut[13, 14] for incompressible flow calculations. The mixed scale model is derived from a class of models which supposed that the subgrid viscosity is a function of the transfer rate, ε, of the kinetic energy, the kinetic energy at the cut-off, $E(k_c)$, and the cut-off wave number, k_c:

$$\mu_t = f\left(\varepsilon, E(k_c), k_c\right). \tag{12}$$

Following a dimensional analysis and assuming a local spectral equilibrium, we may obtain a one parameter family model, written in the physical space as:

$$\mu_t = \bar{\rho} C_M \left\|\bar{\boldsymbol{\omega}}\right\|^{\alpha} \left\|\mathbf{u}''\right\|^{(1-\alpha)} \bar{\Delta}^{(1+\alpha)}, \tag{13}$$

with

$$\left\|\bar{\boldsymbol{\omega}}\right\| = \overline{\omega_{ij}} \cdot \overline{\omega_{ij}}, \tag{14}$$

where $\overline{\omega_{ij}}$ is the vorticity tensor and the Einstein convention is adopted, $\bar{\Delta}$ the implicit filter cut-off length scale related to the mesh size and C_M the model constant that needs evaluation. $\left\|\mathbf{u}''\right\|$ stands for a velocity scale that must be representative of the subgrid scale velocity. Following Bardina et al.[15] about the TKE model, this velocity scale has been related to the subgrid kinetic energy by using a scale similarity assumption. Thanks to an analytical test filter $(\hat{\cdot})$ with a cut-off length scale $\hat{\Delta}$ larger than $\bar{\Delta}$, the subgrid scale velocity is estimated by using the subgrid kinetic energy at the highest resolved wave numbers, q_c:

$$\left\|\mathbf{u}''\right\| = \sqrt{q_c} = \sqrt{\frac{1}{2}\left(\bar{u}_i - \hat{\bar{u}}_i\right) \cdot \left(\bar{u}_i - \hat{\bar{u}}_i\right)}, \tag{15}$$

where the Einstein convention is adopted for the index i of the velocity components u_i. In the following, the explicit test filter is typically expressed using a trapezoidal rule[16] with $\hat{\Delta} = 2\bar{\Delta}$.

The mixed scale model can also be written as the algebraic average of the vorticity model[10] and the TKE model[15]:

$$\mu_{sg} = \left(\underbrace{\bar{\rho} C_\omega^2 \bar{\Delta}^2 \left\| \bar{\boldsymbol{\omega}} \right\|}_{\mu_\omega} \right)^{\alpha} \left(\underbrace{\bar{\rho} C_B \bar{\Delta} \sqrt{q_c}}_{\mu_k} \right)^{1-\alpha} . \tag{16}$$

C_ω and C_B are constants of the vorticity[10] and the TKE[15] models, respectively. In practice, common values of C_ω are: $C_\omega \in [0.1, 0.12]$ [17, 18, 19] and, in order to respect Galilean invariance, $C_B = 1.0$ [15]. Depending on the value of the parameter α, equation (16) becomes either the vorticity model, when $\alpha = 1$, or the TKE model, for $\alpha = 0$. For $0 < \alpha < 1$, the TKE model can therefore be seen as a damping function of the vorticity model. Thanks to this, the subgrid viscosity is then damped smoothly and vanishes in regions where all the scales are well resolved. As a natural value, we have chosen $\alpha = 1/2$, in agreement with simulations carried out with this model so far[14, 20, 21]. Hence, in the following, the presented results have been obtained by setting the model coefficient $C_M = C_S^{2\alpha} C_B^{1-\alpha}$ at its current corresponding value $C_M = 0.04$.

3 NUMERICAL MODELING OF THE DISCRETE PHASE

3.1 Mathematical formulation

The individual motion of particles in the flow is modeled following a Lagrangian approach, where the trajectory of each particle is found by solving a set of ordinary differential equations along its path. This approach is specially suited to model two-phase flows with low particle concentration, high accelerations and with non-uniform properties, as in the present work.

Neglecting rotational effects of the particles, the differential equations used to compute the particle location vector $\mathbf{x}_p$ and velocity vector $\mathbf{v}_p$ of a single particle of mass m_p are:

$$\frac{d\mathbf{x}_p}{dt} = \mathbf{v}_p , \tag{17}$$

$$m_p \frac{d\mathbf{v}_p}{dt} = \sum_i \mathbf{F}_i . \tag{18}$$

All relevant forces $\mathbf{F}_i$ acting upon the particle (admitted to be a sphere of diameter d_p and density ρ_p) must be included in equation (18). In this study, we consider the aerodynamic drag, $\mathbf{F}_D$, the gravity force, $\mathbf{F}_g$, the pressure gradient force, $\mathbf{F}_P$, the transverse lift, $\mathbf{F}_L$ (also known as the Saffman force), the Archimedes force, $\boldsymbol{\Pi}$, and the added mass force, $\mathbf{F}_A$, so that equation (18) becomes:

$$m_p \frac{d\mathbf{v}_p}{dt} = \mathbf{F}_D + \mathbf{F}_g + \mathbf{F}_P + \mathbf{F}_L + \mathbf{\Pi} + \mathbf{F}_A \,. \tag{19}$$

The aerodynamic (friction and pressure) drag is expressed by:

$$\mathbf{F}_D = \frac{3}{4} m_p \frac{\mu}{\rho_p d_p^2} C_D \, Re_p \left(\mathbf{v} - \mathbf{v}_p \right), \tag{20}$$

where the particle Reynolds number is defined as:

$$\mathrm{Re}_p = \frac{\rho_0 \, d_p \left| \mathbf{v} - \mathbf{v}_p \right|}{\mu}, \tag{21}$$

and $\mathbf{v}$, μ and ρ_0 are the carrier fluid velocity, dynamic viscosity and constant density, respectively.

The drag coefficient C_D in equation (20) is computed using the empirical formulation proposed by Wallis[22]:

$$C_D \, Re_p = \begin{cases} 24 & Re_p < 0.5 \\ 24 + 3.6 \, Re_p^{0.687} & 0.5 < Re_p < 1000 \\ 0.44 \, Re_p & Re_p > 1000 \end{cases}. \tag{22}$$

Denoting the acceleration of gravity by $\mathbf{g}$, the gravity and the Archimedes forces:

$$\mathbf{F}_g = m_p \mathbf{g} = \frac{1}{6} \pi \, d_p{}^3 \rho_p \mathbf{g}, \tag{23}$$

$$\mathbf{\Pi} = -\frac{1}{6} \pi \, d_p{}^3 \rho_0 \, \mathbf{g} \tag{24}$$

can be cast into a single expression for the body forces, $\mathbf{F}_B$:

$$\mathbf{F}_B = \frac{1}{6} \pi \, d_p{}^3 \left(\rho_p - \rho_0 \right) \mathbf{g} \,. \tag{25}$$

The force originated by the pressure gradient of the carrier fluid surrounding the particle, ∇P, is:

$$\mathbf{F}_P = -m_p \frac{\nabla P}{\rho_p} \,. \tag{26}$$

The transverse lift is due to the non-uniform relative velocity over the particle and the resulting non-uniform pressure distribution. Following Sommerfeld[23], it is given by:

$$\mathbf{F}_L = \frac{\rho_0}{2} \frac{\pi}{4} d_p^2 \, C_{LS} \, d_p \left[\left(\mathbf{v} - \mathbf{v}_p \right) \times \mathbf{\Omega} \right]. \tag{27}$$

In equation (27), $\boldsymbol{\Omega}$ is the rotational of the flow field at the particle location and the lift coefficient, C_{LS}, is given by:

$$C_{LS} = \frac{4.1126}{\sqrt{Re_S}} f\left(Re_p, Re_S\right), \tag{28}$$

where:

$$Re_S = \frac{\rho_0 d_p^2 |\boldsymbol{\Omega}|}{\mu} \tag{29}$$

and $f\left(Re_p, Re_S\right)$ is a correction function proposed by Mei[24], based on the calculations performed by Dandy and Dwyer[25]:

$$f\left(Re_p, Re_S\right) = \begin{cases} \left(1 - 0.3314\sqrt{\beta}\right) exp\left(-\frac{Re_p}{10}\right) + 0.3314\sqrt{\beta} & 0.1 < Re_p < 40 \\ 0.0524\sqrt{\beta Re_p} & 40 < Re_p < 100 \end{cases}, \tag{30}$$

with $\beta = 0.5(Re_S / Re_p)$.

The added mass force accounts for the acceleration or deceleration of the fluid surrounding the particle. Again following Sommerfeld[23], it is given by:

$$\mathbf{F}_A = 0.5 C_A \rho_0 \frac{m_p}{\rho_p} \frac{d}{dt}\left(\mathbf{v} - \mathbf{v}_p\right), \tag{31}$$

where:

$$C_A = 2.1 - \frac{0.132}{A_C^2 + 0.12}, \tag{32}$$

$$A_C = \frac{\left|\mathbf{v} - \mathbf{v}_p\right|^2}{d_p \left|\frac{d\left|\mathbf{v} - \mathbf{v}_p\right|}{dt}\right|}. \tag{33}$$

Owing to the low particle concentration, a one-way coupling formulation was adopted, thus meaning that the influence of particles upon the carrier fluid flow and inter-particle collisions were not considered in this first approach.

3.2 Numerical solution

Equation (19) was solved using a fourth-order Runge-Kutta numerical integration. The selection of the integration time step, Δt, was based on the local value of the Stokes number, $St = \tau_p / \tau_f$, where τ_p and τ_f are the characteristic particle and fluid response times, respectively. τ_p is given by:

$$\tau_p = -\tau_S \ln\left(1 - \frac{1 - e^{-1}}{1 + \tau_S K_0}\right). \tag{34}$$

In this equation, τ_S is the response time due to the aerodynamic drag force alone:

$$\tau_S = \frac{4}{3}\frac{\rho_p d_p^2}{\mu C_D \mathrm{Re}_p}, \tag{35}$$

and K_0 is a correction factor that accounts for the remaining forces acting on the particle:

$$K_0 = \frac{\sum_{i \neq D} \left|\mathbf{F}_i / m_p\right|}{\left|\mathbf{v}\right|}. \tag{36}$$

On the other hand, τ_f is calculated through:

$$\tau_f = \frac{\delta}{\left|\mathbf{v}\right|}, \tag{37}$$

where δ is a linear dimension which characterizes the local size of the Eulerian grid. If $St << 1$, the particle follows the fluid flow, and the time step used is $\Delta t = \tau_f$; if instead $St \sim 1$ or $St >> 1$, then $\Delta t = \tau_p$. The particle should not be allowed to cross more than one Eulerian cell per time step, Δt, which must also be kept bellow the stability limit for the Runge-Kutta method. Additional details may be found in Oliveira[26].

3.3 LES subgrid influence

In the present simulations, the carrier fluid is air and the particle phase is made of oil (isopropanol) droplets, thus meaning that the particle density is much greater than the carrier fluid density. For these conditions, it is acceptable to ignore the influence that the subgrid scale effects of the carrier fluid LES might have upon the particle trajectory calculations[23].

3.4 Particle-wall collision

After hitting a solid boundary, a particle can adhere to it, rebound or splash. Sikalo[27] showed that there is a critical value, α_{cr}, of the particle impact angle on the wall, α, bellow which the hitting particle adheres to the surface. The critical value is independent of the size of the droplet and depends solely on the Weber number, *We*:

$$\alpha_{cr} = \frac{C}{\sqrt{We}}, \tag{38}$$

where *C* is a property of the droplet fluid. For isopropanol, $C = 104^o$ (cf. Tekam[1]). The Weber number is given by:

$$We = \frac{\rho_p \, d_p \left| \mathbf{v}_p \right|^2}{\sigma}, \tag{39}$$

where σ is the surface tension of the droplet. For isopropanol:

$$\sigma = 23 - 0.0789\,(T - 24) \quad \left[mN/m \right], \tag{40}$$

T being the droplet temperature in ^{o}C.

The impact of oil droplets in walls was simulated using *binary* models proposed by Tekam[1]. These models simulate the rebound/adhesion of the droplet, depending on a critical value, We_{cr}, of the Weber number, We_n, based on the particle velocity component normal to the wall, $\left(\left| \mathbf{v} \right|_p \right)_n$:

$$We_n = \frac{\rho_p \, d_p \left(\left| \mathbf{v}_p \right| \right)_n^2}{\sigma}. \tag{41}$$

If $We_n < We_{cr}$, the droplet rebounds, otherwise it will adhere to the boundary. When a particle rebounds, the velocity after-impact is computed following an energy budget analysis of the collision. A rebound coefficient, r, is then defined to relate the incident, and the rebound particle velocities, $\mathbf{v}_{p,i}$ and $\mathbf{v}_{p,r}$, respectively:

$$\mathbf{v}_{p,r} = r \, \mathbf{v}_{p,i}. \tag{42}$$

Following the proposal of Wang and Watkins[28], which was later tested by Park and Watkins[29], the rebound coefficient is given by:

$$r^2 = 1 - 0.95 \sin^2(\alpha). \tag{43}$$

4 RESULTS

4.1 Description of the test case

The flow configuration adopted here in order to validate the above described numerical method was also used in Tekam's theoretical and experimental study[1]. It consists of an oil decanter equipped with two identical baffles, the dimensions of which are indicated in the schematic representation of figure 1.

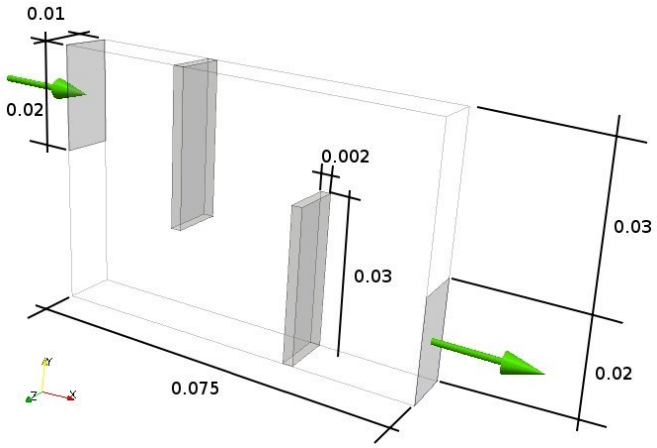

Figure 1: Sketch of the geometry and relevant dimensions (in meter)

The values of the main parameters regarding the continuous phase are summarized in table 1. The Reynolds number, Re, is based on the equivalent hydraulic diameter of the inlet section. The inlet fluid velocity, $\mathbf{v}_{in}$, is aligned with the x axis.

ρ_0	0.946	$kg.m^{-3}$
μ	2.18e-5	$kg/m.s^{-1}$
υ	2.304e-5	$m^2.s^{-1}$
$\lvert\mathbf{v}\rvert_{in}$	1.0	$m.s^{-1}$
Re	578.593	

Table 1: Main parameter values for the continuous phase

Particles (oil droplets) were injected at the inlet with the same velocity as the carrier fluid (air). The injection of particles started at an instant t_0 for which enough time had elapsed for the main turbulent structures of the airflow to be already established. Oil droplets were then introduced into the domain at a constant mass rate, during a pre-defined time interval, Δt_p. Each oil droplet was injected at a randomly chosen location of the inlet section. The values of the main parameters that characterize the dispersed phase are summarized in table 2.

ρ_p	795	$kg.m^{-3}$
d_p	5	μm
$\lvert\mathbf{v}_p\rvert_{in}$	1.0	$m.s^{-1}$

Table 2: Main parameter values for the dispersed phase

The efficiency of the decanter is assessed by comparing the particulate mass flow that left the domain, m_{out}, and the one that is injected, m_{in}, during the same time interval, Δt_p. An efficiency coefficient, η, is then defined as:

$$\eta = \frac{m_{in} - m_{out}}{m_{in}}. \tag{44}$$

Particle-wall interaction is simulated using isopropanol properties. The values of the relevant parameters for the particle impact model described in section 3.4 are indicated in table 3. The value for the critical Weber number was taken from reference data[1] as being representative of real conditions.

C	104	
σ	$23 \times 0.0789(T-24)$	$[mN/m]$
We_{cr}	1	

Table 3: Main parameter values for the particle-wall interaction model

For the present preliminary study, a (*x,y,z*) regularly spaced Eulerian mesh with ($450 \times 100 \times 20$) nodes was used to discretize the flow domain. This numerical grid was chosen in order to ensure a spatial resolution of *0.5mm*, approximately corresponding to a grid spacing of about *2* wall units. The outlet boundary of the calculation domain was artificially displaced downwards, in order to avoid dealing with numerical problems due to the flow recirculation that occurs near the exit section of the decanter. Figure 3 shows the discretization mesh that was used in the simulations.

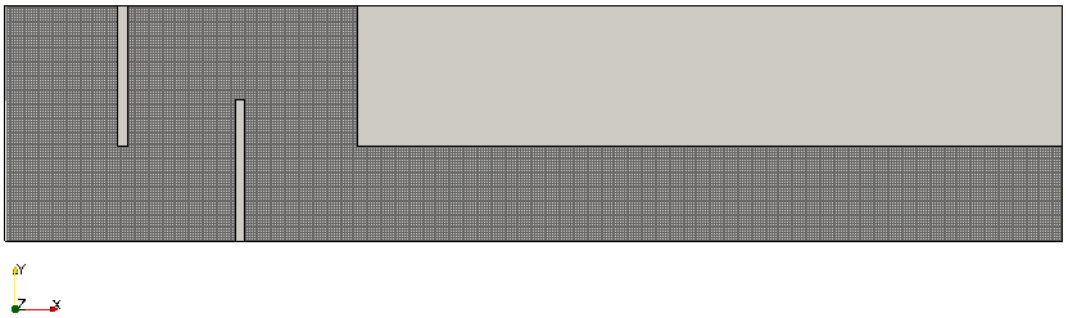

Figure 3: The *900,000* elements $(450 \times 100 \times 20)$ discretization mesh

4.2 Results discussion

The first flow calculations in this work were performed without particles and using a numerical domain that coincides with the decanter volume (no duct extension at the outlet). Considering the configuration of the decanter, a high level of vorticity is generated by the presence of the baffles and is advected by the main flow towards the exit of the domain. Moreover, a separated flow arises downstream of the second baffle. This large unsteady vortex sharply interacts with the outlet boundary conditions which are not commonly defined to manage the presence of intense vortices. As a consequence, the strong influence of the outlet boundary conditions badly affects the flow features. This point will be discussed in more detail at the conference. In order to overcome this problem, the outflow boundary has been displaced, so that the domain is artificially extended to include an exit duct, as represented in figure 3. Calculation can thus provide a better prediction of the flow characteristics, showing that a high level of vorticity is actually present in the vicinity of the decanter outlet section, as is discussed in the following paragraphs.

In fact, the LES results for the continuous phase show that the large eddy motion plays a noticeable role in the flow features and can affect the particule transport, particularly in the second part of the decanter, between the second baffle and the outlet, where the turbulence intensity is higher (see figure 7). As this large eddy motion cannot be easily modeled by a usual RANS procedure, we expect a better performance of the LES approach.

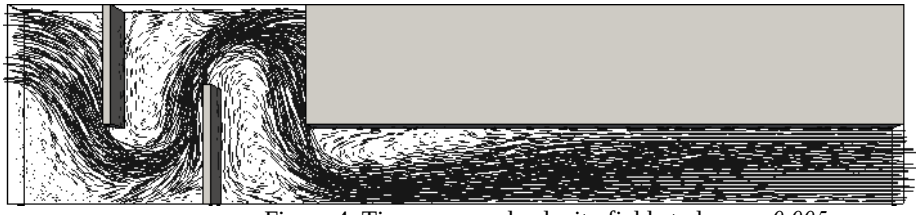

Figure 4: Time-averaged velocity field at plane *z=0.005m*

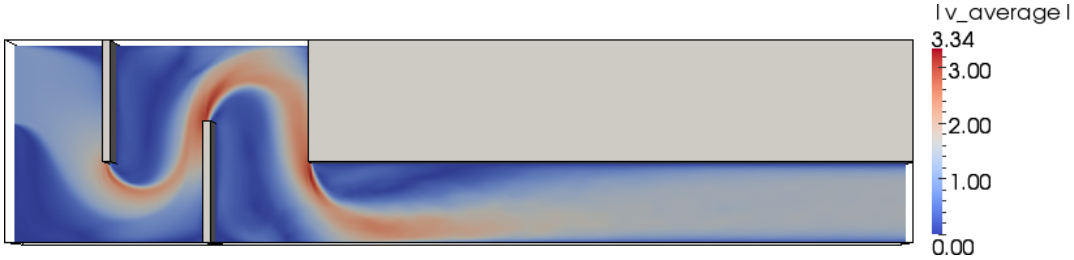

Figure 5: Time-averaged velocity field magnitude at plane *z=0.005m*

Figures 4 and 5 show the time averaged airflow velocity field and its magnitude $|\overline{\mathbf{v}}|$, respectively, within a domain section located at the mid-plane.

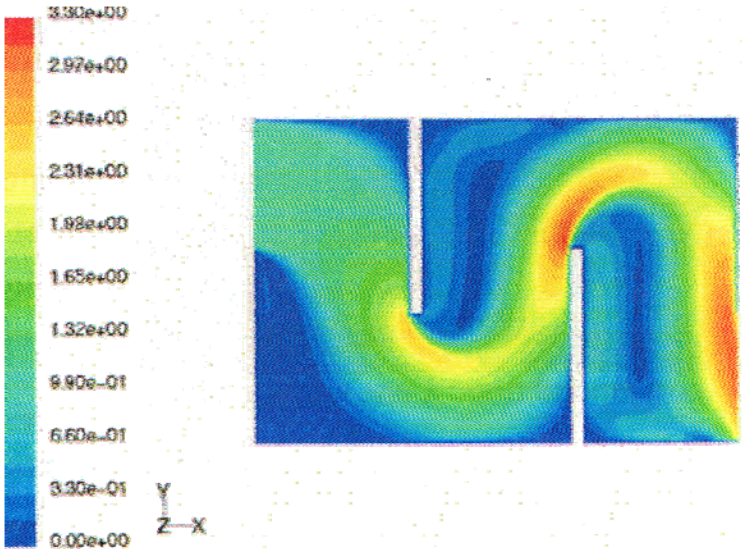

Figure 6: Tekam's results corresponding to those shown in figure 4 (see [1])

The corresponding results obtained by Tekam[1], using a RANS formulation, together with a $k-\varepsilon$ turbulence model, are shown in figure 6. From a qualitative viewpoint, general agreement is seen to hold between the present results for the time averaged velocity distribution and those obtained by Tekam. However, as opposed to the present calculations, no recirculation was predicted by this author for the region close to the decanter outlet section. This might be due to the RANS procedure coupled with the

wrong effect of the outlet boundary conditions, which are defined without duct extension.

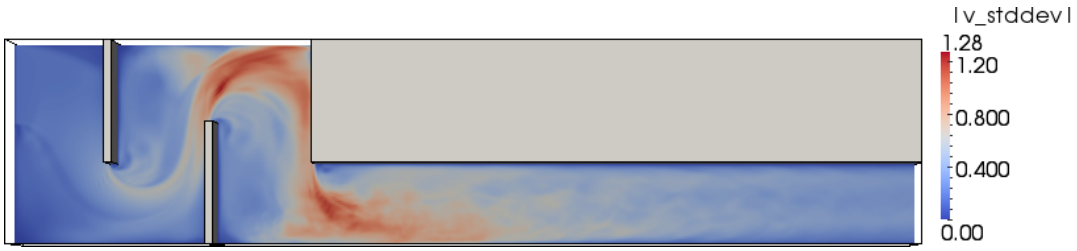

Figure 7: Standard deviation of time-averaged velocity field magnitude at plane *z=0.005m*

In figure 7, the standard deviation distribution of the time-averaged velocity field is shown for the plane section of figures 4 and 5. A high level of fluctuation is observed in the vicinity of the decanter exit. Again, this explains the need of knowing in detail the flow structure and its unsteady behavior beyond the outlet of the decanter. That knowledge improves the flow description and more specifically the separated flow prediction in the decanter outlet region.

Once the continuous phase flow was well established, particles were then permanently released during a time interval defined by $0 \le t - t_0 \le \Delta t_p$, with $\Delta t_p = 0.04\,s$. An illustration including sample particle trajectories is shown in figure 8. Some droplets are seen to follow the main flow, while others are trapped within different flow recirculation structures.

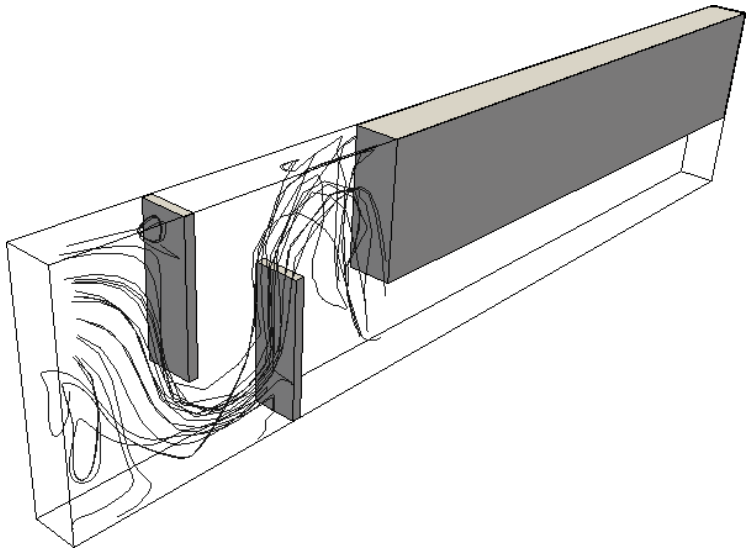

Figure 8: Sample trajectories of particles that were injected at *x=0,* in the plane *z=0.005m*

Figure 9 shows the variation with time of the decanter efficiency, η, as defined in section 4.1. The duration of the initial phase, for which $\eta \cong 1$, corresponds to the time interval that is typically taken by a particle to go through the whole decanter, from inlet to exit.

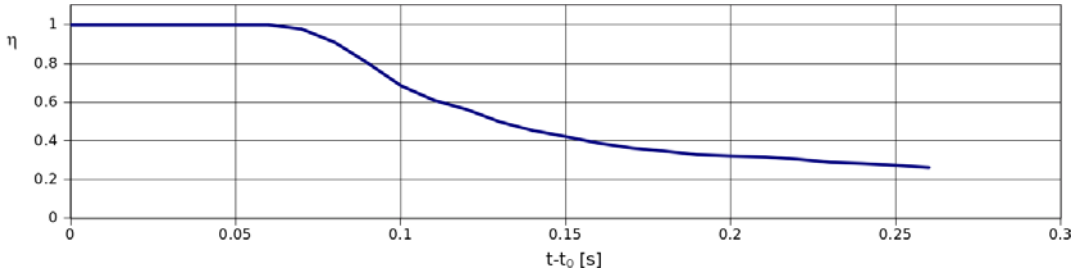

Figure 9: Time variation of the decanter efficiency, η

Despite the discrepancies on the velocity field, mainly close to the outlet, the asymptotic value of η seems to converge toward the range recorded by Tekam[1], from *5 %* to *30 %* depending on the grid refinement used (lower values corresponding to more refined grids). However, the present efficiency coefficient still evolves and more detailed results will be presented at the conference. A close quantitative agreement should however not be expected, considering the above mentioned ability of the LES to take into account the highly fluctuating character of the carrier fluid flow (in particular within the close vicinity of the decanter exit), together with the influence exerted by that behavior upon the dynamics of the particulate phase.

5 CONCLUSIONS

In this work, we have successfully simulated the transport of oil droplets inside a decanter, by following a LES approach for the airflow coupled with a Lagrangian method for the dispersed phase, including a particle-wall interaction modeling. Even though these are only preliminary results of recently started research, the first comparisons that were established with published data are encouraging. More specifically, we have pointed out the need of taking into account in detail the unsteady behavior of the flow and its structure, which can affect the particulate transport. Moreover, it is relevant to shift the outflow boundary conditions downstream the decanter outlet in order to avoid any harmful disturbance on the flow features.

Future developments will include a more elaborate model for particle motion, by taking into account a number of relevant features, namely the inclusion of:

- two-way coupling effects between the continuous phase and the dispersed phase;
- LES subgrid scale effects on particles;
- a modified drag coefficient as a function of the distance to walls as was proposed by Risk [30];
- particle rotation and sphericity;
- collisions between particles;
- surface roughness influence in the impact model;
- rarefaction effects through a Brownian force, which is important for particle diameters lower than $0.5\mu m$.

The dependence of the decanter efficiency as a function of the droplet characteristics (namely their diameter) will also be addressed. Results on that issue should be available for the oral presentation of this work.

REFERENCES

[1] S. M. Tekam, Modélisation et simulation numérique d'écoulements gazeux chargés de particules d'huile dans un circuit de décantation de moteur, PhD thesis report*, Ecole Nationale Supérieure d'Arts et Métiers, Paris* (2006).

[2] J.-L. Guermond, P. Minev and J. Shen, An overview of projection methods for incompressible flows, *Comput. Methods Appl. Mech. Engrg.*, **195**, Issues 44-47, 6011–6045 (2006).

[3] C. T. Crowe, T. R. Troutt and J. N. Chung, Numerical models for two-phase turbulent flows, *Annual Review of Fluid Mechanics*, **28**, 11–43 (1996).

[4] L. D. Fan and C. Zhu, Principles of Gas–Solid Flows, *Cambridge University Press: Cambridge*, *U.K.*, (1998).

[5] X. Baby, Optimization de l'aérodynamique interne dans un moteur à injection directe essence. Analyse de l'écoulement de thumble par vélocimétrie par images de particules, PhD thesis report, *RENAULT*, *IMFT* (2000).

[6] M. D. Wang and A. P. Watkins, Numerical modeling of diesel spray wall impaction phenomena, *International Journal of Heat and Fluid*, **14**, 301-312 (1993).

[7] E. Gadoin, P. Le Quéré and O. Daube, A general methodology for investigating flow instability in complex geometries: Application to natural convection in enclosures, *Int. J. Num. Meth. in Fluids*, **37**, 175–208 (2001).

[8] C. Hirsch, Numerical computation of internal and external flows, *A Wiley interscience publication, Wiley & Sons edition*, **Vol. I** (1987).

[9] J. Smagorinsky, General circulation experiments with the primitive equations I: The basic experiments, *Month. Weath. Rev.*, **91 (3)**, 99–165 (1963).

[10] N. N. Mansour, J. H. Ferziger and W. C. Reynolds, Large eddy simulation of a turbulent mixing layer, Report TF 11, *Thermosciences Div, Dept of Mech. Eng., Standford University, CA*, (1978).

[11] M. Germano, U. Piomelli, P. Moin and W. H. Cabot, A dynamic subgrid-scale eddy viscosity model, *Physics of Fluids A: Fluid Dynamics*, **3**, 1760–1765 (1991).

[12] L. Ta Phuoc, Aérodynamique instationnaire turbulente - aspects numériques et exerimentaux, *Journée thématique DRET* (1994).

[13] P. Sagaut, Simulations numériques d'écoulements décollés avec des modèles de sous-maille, PhD thesis, *Université Pierre & Marie Curie (Paris VI)*, (1995).

[14] P. Sagaut, Introduction de la simulation des grandes échelles pour les écoulements de fluide incompressible, *Springer-Verlag* (1998).

[15] J. Bardina, J. H. Ferziger and W. C. Reynolds, Improved subgrid scale models for large eddy simulation, *AIAA Paper*, 80-1357 (1980).

[16] S. Liu, C. Meneveau and J. Katz, On the propeties of similarity subgrid scale models as deduced from measurements in a turbulent jet, **275**, 83–119 (1994).

[17] J. W. Deardorff, A numerical study of three-dimensional turbulent channel flow at large reynolds numbers, *Journal of Fluid Mechanics*, **41 (2)**, 453–480 (1970).

[18] C. Meneveau, Statistics of turbulence subgrid-scale stresses: Necessary conditions and experimental tests, *Physics of Fluids*, **6 (2)**, 815–833 (1994).

[19] J. O'Neil and C. Meneveau, Subgrid scale stresses and their modelling in a turbulent plane wake, *Journal of Fluid Mechanics*, **349**, 253–293 (1997).

[20] E. Lenormand, P. Sagaut, L. Ta Phuoc and P. Comte, Subgrid-scale models for large-eddy simulations of compressible wall bounded flows, *AIAA Journal*, **38 (8)**, 1340–1350 (2000).

[21] C. Tenaud and L. Ta Phuoc, LES of unsteady compressible separated flow around NACA 0012 airfoil, In P. Kutler, J. Flores, and J.J. Chattot, editors, *Lecture Notes in Physics*, **Vol. 490**, 424–429, *15th International Conference on Numerical Methods in Fluid Dynamics*, Monterey, CA, June 1996, (1997).

[22] G. B. Wallis, One Dimensional Two-Phase Flow, *McGraw Hill*, (1969).

[23] M. Sommerfeld, B. Wachem and R. Oliemans, Best practice guidelines for computational fluid dynamics of dispersed flows, *ERCOFTAC* (2008).

[24] R. Mei, An approximate expression for the shear lift force on a spherical particle at finite Reynolds number, *Int. J. Multiphase Flow*, **18**, 145-147 (1992)

[25] D. S. Dandy and H. A. Dwyer, A sphere in shear flow at finite Reynolds number : Effect of shear on particle lift, drag, and heat transfer, *J. Fluid Mech.*, **Vol. 216**, 381-410 (1990).

[26] L. A. Oliveira, V. A. F. Costa and B. R. Baliga, Numerical model for the prediction of dilute three-dimensional, turbulent fluid-particle flows, using a Lagrangian approach for particle tracking and a CVFEM for the carrier phase, *Int. J. Numer. Meth. Fluids, 2008,* **58**, 473-491 (2008).

[27] S. Sikalo, M. Marengo, C. Tropea and E. N. Ganié, Analysis of impact of droplets on horizontal surfaces, *Experimental Thermal and Fluid Sciences*, (2005).

[28] D. M. Wang and A. P. Watkins, Numerical modeling of diesel spray wall impaction phenomena, *International Journal of Heat and Fluid*, (1993)

[29] K. Park and A. P. Watkins, Comparison of wall spray impaction models with experimental data on drop velocities and sizes, *International Journal of Heat and Fluid*, (1996)

[30] M. A. Risk and S. E. Elghobashi, The motion of a spherical particle suspended in a turbulent flow near a plane wall, *Physics and Fluids*, **28 (3)**, 806-817 (1985).